Impedance Based Characterization of a High-Coupled Screen Printed PZT Thick Film Unimorph Energy Harvester

Anders Lei, Ruichao Xu, Louise M. Borregaard, Michele Guizzetti, Ole Hansen, and Erik V. Thomsen

***Abstract*— The single degree of freedom mass-spring-damper system is the most common approach for deriving a full electromechanical model for the piezoelectric vibration energy harvester. In this paper, we revisit this standard electromechanical model by focusing on the impedance of the piezoelectric device. This approach leads to simple closed form expressions for peak power frequency, optimal load, and output power without a tedious mathematical derivative approach. The closed form expressions are validated against the exact numerical solution. The electromechanical model contains a set of only five lumped parameters which, by means of the piezoelectric impedance expression, all can be determined accurately by electrical measurements. It is shown how four of five lumped parameters can be determined from a single impedance measurement scan, considerably reducing the characterization effort. The remaining parameter is determined from shaker measurements, and a highly accurate agreement is found between model and measurements on a unimorph MEMS-based screen printed PZT harvester. With a high coupling term $K^2 Q \simeq 7$, the harvester exhibits two optimum load points. The peak power performance of the harvester was measured to 11.7 nW at an acceleration of 10 m*g* with a load of 9 kΩ at 496.3 Hz corresponding to 117 μW/g^2. [2013-0097]**

***Index Terms*— Energy harvesting, vibration harvesting, MEMS, PZT, PZT thick film, screen printing.**

I. Introduction

DRIVEN by significant advances in low power electronics and especially sensor units such as gyroscopes and accelerometers, numerous autonomous wireless sensor systems have emerged in the past decade. Regardless of whether the sensor systems are used for industrial monitoring or consumer products, they rely on a compact lightweight energy source which in practice is synonymous with an electrochemical battery. This choice of energy source though limits either the lifespan or the size of the sensor system. For this reason, the field of power harvesting on a micro-scale has grown rapidly. The motivation is straightforward; attain a fully self-sustained wireless sensor system by replacing the electrochemical battery with a small self-sufficient power source. Of the most common ambient sources of energy: thermal energy, light, RF radiation and vibrations/motions [1], the latter is of high interest since it is inherently present on moving objects and it provides a reasonable constant source of energy. Harvesting energy from vibrations usually employs an electrostatic, electromagnetic or piezoelectric transducer mechanism [2], [3]. The piezoelectric harvester, which utilises stress induced in a piezoelectric layer due to bending of a suitable structure, has gained much attention in literature due to high coupling efficiency and simple design enabling a high degree of miniaturisation [4].

Together with the efforts in development and fabrication of piezoelectric harvesting devices, the field of modelling has developed accordingly. Full distributed models have been presented and verified [5]–[8], and while these models can accurately capture the harvester behaviour at several different modes, the models are less intuitive for direct parameter analysis and experimental fitting. In real applications only the behaviour of the harvester near the fundamental resonance is of interest and then much simpler models can be developed. By considering the mechanics of the harvester as a single degree of freedom (SDOF) mass-spring-damper system, the full electromechanical behaviour of the harvester can be described by a set of lumped parameters.

Independent on modelling approach, the model accuracy relies on precise values for the geometrical, mechanical and electrical parameters all of which may have tolerances that complicate precise analytic predictions in relation to measurements. Secondly, regardless of the model, the highly crucial damping term cannot yet be predicted analytically and must be determined experimentally. Consequently it is often desirable to precisely identify the model parameters from the harvester characterisation process.

The lumped model can describe the harvester performance using only five parameters which all can be easily determined experimentally. While this determination often is conducted using the direct piezoelectric effect by means of a shaker [9],

Manuscript received April 4, 2013; revised August 19, 2013 and December 3, 2013; accepted December 7, 2013. Date of publication January 13, 2014; date of current version July 29, 2014. This work was supported in part by the Danish National Advanced Technology Foundation through the ELiminating BAtteries project-energy harvesters for integrated systems under Contract 036-2009.1, and in part by the Center for Individual Nanoparticle Functionality (CINF) through the Danish National Research Foundation under Grant DNRF54. Subject Editor S. M. Spearing.

A. Lei and E. V. Thomsen are with the Department of Micro- and Nanotechnology, Technical University of Denmark, DTU Nanotech, Kgs. Lyngby 2800, Denmark (e-mail: anders.lei@nanotech.dtu.dk; erik.thomsen@nanotech.dtu.dk).

R. Xu, L. M. Borregaard, and M. Guizzetti are with Meggitt A/S, Kvistgaard 3490, Denmark (e-mail: ruichao.xu@meggitt.com; louise.borregaard@meggitt.com; michele.guizzetti@meggitt.com).

O. Hansen is with the Department of Micro- and Nanotechnology, Technical University of Denmark, DTU Nanotech, Kgs. Lyngby 2800, Denmark, and also with CINF, Technical University of Denmark, Kgs. Lyngby 2800, Denmark (e-mail: ole.hansen@nanotech.dtu.dk).

Color versions of one or more of the figures in this paper are available online at http://ieeexplore.ieee.org.

Digital Object Identifier 10.1109/JMEMS.2013.2295625

this work utilises mainly the indirect piezoelectric effect. With the SDOF model, the piezoelectric device impedance can readily be expressed in terms of the lumped parameters and consequently four out of five parameters needed to model the harvester can be extracted directly. Instead of using the common approach of analysing the full power expression to identify the optimal load conditions and peak power frequencies, we use the expression for the piezoelectric device impedance. The approximations used for the simple closed form expressions are verified by comparison with the exact solutions solved numerically. Excellent agreement is observed for low-coupled systems with only one optimal operating point, while it is shown that the output power becomes equal to the available power of the resonator for higher coupled systems where two optimal operating points with equal output power exist [9].

The lumped parameter model is experimentally verified by characterisation of a high coupled unimorph energy harvester. The literature describes numerous energy harvester prototypes but while the majority of these are proof of concept devices with the purpose of validating theory, only a minor number of the reported energy harvesters‘ [10]–[13] are potentially interesting from an application point of view where small dimensions combined with low frequency are the success criteria. The harvester presented in this work is fabricated using MEMS-technology providing the necessary tools to obtain a small device with resonant frequency in the interesting range [14]. The harvester is based on screen-printed PZT, a technique that is widespread and well tested. Screen-printing of PZT offers better high volume fabrication possibilities compared to bulk PZT and it provides considerably thicker layers compared to sol-gel and sputtering methods [15].

The article is organised as follows. The full electromechanical model is revisited followed by closed form approximated peak power frequency, optimal load and output power expressions for low and high-coupled harvesters. Next, the closed form expressions are validated by a comparison with the exact numerical solutions. Then the wafer-level fabrication of the high-coupled energy harvester with screen printed PZT thick film is presented. The fabricated harvester is characterised and it is shown that the SDOF lumped model accurately represents the harvester performance and how all five lumped parameters can be extracted experimentally by fitting to the closed form expressions.

II. MODELING

A. SDOF System and Equivalent Circuit

The unimorph energy harvester is modelled as a lumped parameter SDOF oscillator with the equivalent circuit diagram shown in Fig. 1. The mechanical domain holds the lumped elements of the spring-mass-damper system with the effective mass m_{eff} represented by an inductor, the spring constant k_{c} as a capacitor and a resistor representing the damping coefficient b of the oscillator. F_{ext} is the external driving force acting on the cantilever and is represented as a voltage source, and the velocity of the centre of mass, $\dot{w}_{\text{c}}$, is the analogue to the current I. F_{piezo} is the back-coupled force from the piezoelectric layer to the mechanical domain. The electrical domain consist of the generated voltage V over the piezoelectric capacitor C.

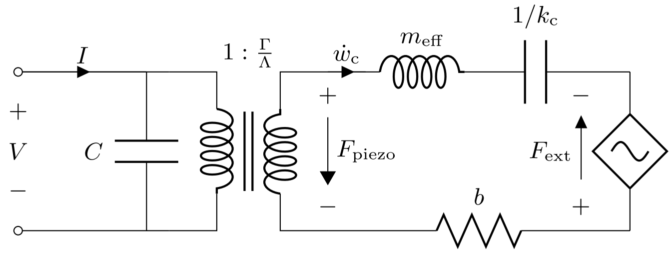

Fig. 1. Equivalent circuit diagram for the unimorph energy harvester. The electromechanical coupling between the electrical and mechanical domains is represented by an ideal transformer.

The electromechanical coupling between the mechanical and electrical domains is represented by an ideal transformer with a transformation factor of $1 : \Gamma/\Lambda$. The Γ part of the transformation factor is the coupling coefficient relating both the current I with the deflection slope rate $\dot{w}_c'$, and the back-coupled induced moment with voltage as described by (23) in the Appendix. Λ is a geometric length factor relating $\dot{w}_c'$ with $\dot{w}_{\text{c}}$, see (24) in Appendix. Accordingly, the back-coupled force acting on the cantilever can be expressed by $F_{\text{piezo}} = V\Gamma/\Lambda$. By analysing the mechanical loop using Kirchoff's voltage law, the following equivalent Laplace transformed vertical force balance equation emerges

$$F_{\text{ext}} + \frac{\Gamma}{\Lambda}V = Z_{\text{m}}\dot{w}_{\text{c}}, \tag{1}$$

where $Z_{\text{m}} = sm_{\text{eff}} + b + k_{\text{c}}/s$ is the mechanical impedance of the spring-mass-damper system and $s = j\omega$ is the complex frequency.

In the electrical domain the current flowing into the transducer can be found by Kirchoff's current law as

$$I = \frac{\Gamma}{\Lambda}\dot{w}_{\text{c}} + sCV. \tag{2}$$

With the energy harvester connected to an external load resistor R_l, the current in (2) can be expressed as $I = -V/R_l$ and then the voltage can be deduced to

$$V = -F_{\text{ext}}\frac{(\Gamma/\Lambda)\,R_l}{(\Gamma/\Lambda)^2\,R_l + (sCR_l+1)\,Z_{\text{m}}}. \tag{3}$$

The resulting power dissipated in the connected resistive load is

$$P = \frac{|V_{\text{RMS}}|^2}{R_l} = \frac{\left|F_{\text{ext,RMS}}\right|^2}{R_l}\frac{(\Gamma/\Lambda)^2}{\left|(\Gamma/\Lambda)^2 + Z_{\text{m}}/Z_{\text{e}}\right|^2} \tag{4}$$

where

$$Z_{\text{e}} = \frac{R_l}{1+sCR_l} \tag{5}$$

is the electrical impedance of the connected load and piezoelectric capacitor.

B. Optimal Load and Peak Power

The usual approach to accurately determine the optimal load value and frequency for maximum output power is to differentiate the power expression in (4) with respect to both R_l and ω simultaneously. Solving this requires a highly complex mathematical treatment [16], and the importance of the various parameters is easily missed. Other works involve either focusing on the damping term [9] or differentiating the power with respect to load resistance [17]. Both procedures require assumptions concerning operating frequencies and the physical interpretation is less evident. Instead of solving the power expression in (4), the focus in the following analysis is the piezoelectric device impedance from which both an approximate analytic solution can be deduced and also the correct numerical values.

The piezoelectric device impedance Z can from the Thevenin-Norton source transformation theorem be determined from $Z = V_{\mathrm{oc}}/I_{\mathrm{sc}}$, where V_{oc} is the open circuit voltage, and I_{sc} the short-circuit current. Expressions for both can be derived from the voltage in (3) and the piezoelectric device impedance can hence be expressed as

$$Z = \frac{Z_{\mathrm{m}}}{(\Gamma/\Lambda)^2 + CsZ_{\mathrm{m}}}. \tag{6}$$

The damping coefficient in the mechanical impedance can be expressed in terms of a mechanical quality factor Q by the relation

$$Q = k_{\mathrm{c}}/(b\omega_0) = m_{\mathrm{eff}}\omega_0/b = \sqrt{m_{\mathrm{eff}}k_{\mathrm{c}}}/b, \tag{7}$$

where ω_0 is the angular mechanical resonant frequency. The system coupling coefficient, also often referred to as the generalised electromechanical coupling (GEMC) coefficient [18], is expressed by

$$K^2 = (\Gamma/\Lambda)^2/(k_{\mathrm{c}}C). \tag{8}$$

Using the definition for the effective mass ($\omega_0 = \sqrt{k_{\mathrm{c}}/m_{\mathrm{eff}}}$) in combination with (7) and (8) the impedance in (6) can be expressed as

$$Z = -\frac{j}{\omega_0 C}\frac{j\frac{\omega}{\omega_0} + Q\left(1 - \frac{\omega^2}{\omega_0^2}\right)}{\frac{\omega}{\omega_0}\left[j\frac{\omega}{\omega_0} + Q\left(1 - \frac{\omega^2}{\omega_0^2}\right) + QK^2\right]} \tag{9}$$

and hence the impedance of the harvester can be determined by the capacitance C, resonant frequency $f_{\mathrm{r}} = \omega_0/(2\pi)$, system coupling coefficient K and mechanical quality factor Q without information on the coupling transformation factor Γ/Λ or effective mass m_{eff}.

The phase angle θ of the impedance Z is very important for understanding the behaviour of the harvester as explained below. The phase angle can be calculated by recognizing that $\tan\theta = \mathrm{Im}(Z)/\mathrm{Re}(Z)$, and by use of (9) the phase angle becomes

$$\theta = \arctan\left(\frac{\omega}{\omega_0}\frac{Q^2K^2+2Q^2-1}{QK^2} - \frac{\omega_0}{\omega}Q\frac{K^2+1}{K^2} - \frac{\omega^3}{\omega_0^3}\frac{Q}{K^2}\right). \tag{10}$$

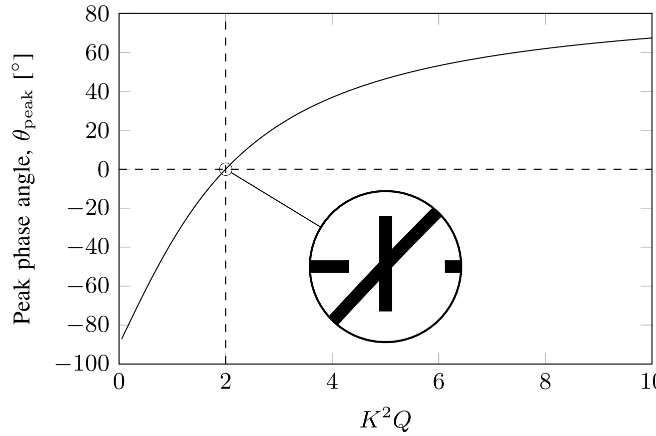

Fig. 2. Peak phase angle of the piezoelectric device impedance (12b) as function of the figure of merit term K^2Q. The horizontal dashed line indicates zero phase angle while the vertical dashed line indicates the zero phase angle/real impedance condition $K^2Q = 2$ where the phase angle becomes positive.

Maximum power is transferred when the impedance of the connected load Z_l equals the complex conjugate of the piezoelectric impedance ($Z_l = Z^*$) [19]. Since the load is a resistance $Z_l = R_l$, it is evident that impedance matching can only occur when the piezoelectric device impedance is purely real which corresponds to a phase angle of zero degrees for the impedance in (9). This zero phase angle condition can be examined using the expression for the peak phase angle θ_{peak} of the impedance, which is obtained by the condition of zero frequency derivative of the argument in the phase angle expression (10). This results in the frequency of peak phase ω_{pp}

$$\left(\frac{\omega_{\mathrm{pp}}}{\omega_0}\right)^2 = \frac{1}{6}\left(2 + K^2 - \frac{1}{Q^2} + \sqrt{12\left(K^2+1\right) + \left(2 + K^2 - \frac{1}{Q^2}\right)^2}\right) \tag{11}$$

and when this frequency is inserted in (10), an expression for the peak phase angle results

$$\theta_{\mathrm{peak}} \simeq \arctan\left(-\sqrt{\frac{2}{2+K^2}}\frac{4+2K^2-K^4Q^2}{4K^2Q}\right) \tag{12a}$$

$$\simeq \arctan\left(-\frac{4-K^4Q^2}{4K^2Q}\right) \tag{12b}$$

where (12b), which is plotted in Fig. 2, is valid for sufficiently high Q. As readily apparent from both (12b) and the inset and dashed lines in Fig. 2, the peak phase angle is zero ($\theta_{\mathrm{peak}} = 0$) at the condition $K^2Q \approx 2$ and load matching is accordingly possible as the piezoelectric impedance becomes real. When $K^2Q > 2$ the peak phase angle becomes positive and consequently there must be two different operating conditions at which $\theta = 0$ and load matching with the resistive load can occur. When on the other hand $K^2Q < 2$, the peak phase angle is negative hence complex conjugate impedance matching with a resistive load is not possible.

The impedance in (9) becomes real at angular frequencies ω_{real} where the phase angle in (10) becomes zero, and thus

$$\left(\frac{\omega_{\text{real}}}{\omega_0}\right)^2 = \frac{1}{2}\left(2 + K^2 - \frac{1}{Q^2} \pm\sqrt{\left(K^2 - \frac{1}{Q^2}\right)^2 - \frac{4}{Q^2}}\right) \quad (13)$$

which is in accordance with the results of Renno *et al.* [16]. Obviously, ω_{real} becomes purely real if

$$K^2 Q - \frac{1}{Q} \geq 2. \quad (14)$$

From (12b) and (14) it is clear that the term K^2Q has a strong impact on the harvesters load and peak power frequency characteristics, and K^2Q is thus often referred to as a coupling efficiency figure of merit (FOM) [9], [16], [17], [20]. It should be noted that the peak phase angle plotted in Fig. 2 is a rapid approach for determining this important coupling efficiency FOM experimentally from a simple impedance measurement.

In the following it is desirable to divide the harvester analysis into three cases: 1) the branching point case where $K^2Q = 2 + 1/Q$, 2) the low-coupled case, with $K^2Q < 2$, and 3) the high-coupled case with $K^2Q > 2$.

1) Branching Point Case $K^2Q = 2 + 1/Q$: In this case, the analysis is particularly simple, and exact solutions are easily obtained. Complex conjugate impedance matching of the resistive load is possible at a single angular frequency $\omega_{\text{bp}} = 2\pi f_{\text{bp}}$, where the piezoelectric device impedance is purely real (in this case the phase is maximized at the same frequency). From (13) the matching frequency is easily obtained

$$\left(\frac{\omega_{\text{bp}}}{\omega_0}\right)^2 = \frac{1}{2}\left(2 + K^2 - \frac{1}{Q^2}\right) = \left(1 + \frac{1}{Q}\right), \quad (15)$$

and at that frequency the piezoelectric device impedance is

$$Z = R_{l\text{bp}} = \frac{1}{\omega_0 C}\frac{1}{1 + 1/Q} \simeq \frac{1}{\omega_0 C}, \quad (16)$$

where the approximation is valid at sufficiently high Q. Since complex conjugate load matching is achieved, the peak harvested power equals the available power P_{av} [4], [21], [22]

$$P_{\text{av}} = \frac{\left|F_{\text{ext,RMS}}\right|^2}{4b} = \frac{\left|F_{\text{ext,RMS}}\right|^2}{4\omega_0 m_{\text{eff}}}Q, \quad (17)$$

as is verified by using $R_{l\text{bp}}$ and ω_{bp} in the output power expression (4).

2) Low-Coupled Case $K^2Q < 2$: In this case complex conjugate load matching is not possible. The peak power point is instead found at the angular frequency $\omega_{\text{pp}} = 2\pi f_{\text{pp}}$ (11) where the phase of the piezoelectric device impedance is maximized, i.e. the frequency derivative of the phase angle in (10) becomes zero

$$\left(\frac{\omega_{\text{pp}}}{\omega_0}\right)^2 \simeq 1 + \frac{1}{2}K^2, \quad (18)$$

where the approximation is valid at sufficiently high quality factor ($Q > 100$) and small coupling coefficient ($K < 0.4$). The frequency in (18) agrees with that of [16] which is based on a mathematical derivative approach. A comparison with the relation between the resonant and anti-resonant frequencies $f_{\text{a}} = f_{\text{r}}\sqrt{1 + K^2}$ reveals that the peak phase frequency in (18) is approximately midway between the resonant and anti-resonant frequencies (note, the resonant and anti-resonant frequencies are the system eigen-frequencies with the electrical side in short and open circuit, respectively). In this case the optimal load resistance is approximately the same as in the branching point case $R_{l\text{pp}} \simeq 1/(\omega_0 C)$, and when these conditions are inserted into the output power expression (4), the output power can to a good approximation be described by

$$P_{\text{p}} = P_{\text{av}}\frac{8K^2Q}{4 + K^4Q^2 + 4K^2Q} \equiv P_{\text{av}}\chi, \quad (19)$$

where χ is a power multiplication factor for the low-coupled regime. The power approximation agrees with the findings of Guyomar *et al.* [23] under identical load conditions.

3) High-Coupled Case $K^2Q > 2$: In this case the harvester should not be operated at the peak phase point as in the low-coupled system, instead the optimal operating points are the two points (frequencies) where the phase is zero degrees ($\theta = 0$). These frequencies are obtained directly from (13); if the negative sign in (13) is chosen, a frequency f_{pr} close to the resonant frequency is obtained, whereas if the positive sign is chosen in (13) a frequency f_{pa} close to the anti-resonant frequency obtains. The impedance (which is real) of the piezoelectric harvester at the two frequencies is calculated

$$Z = R_{l\text{opt}} = \frac{1}{\omega_0 C}\frac{2}{K^2Q + \frac{1}{Q} \mp \sqrt{\left(K^2Q - \frac{1}{Q}\right)^2 - 4}}, \quad (20)$$

where the positive sign yields the impedance and optimal load resistance $R_{l\text{r}}$ at f_{pr} near the resonant frequency, whereas the negative sign yields the impedance and optimal load resistance $R_{l\text{a}}$ at f_{pa} near the anti-resonant frequency. Obviously the optimal load resistance is higher at f_{pa} than at f_{pr}. Since complex conjugate matching is obtained in both cases identical output powers, equal to the available power P_{av}, are expected.

Finally, it should be noted, that in the high-coupled case a local minimum in the output power exists at the peak phase frequency f_{pp} which can be obtained from (18) and in this condition the output power is also well described by (19).

C. Numerical Analysis

The graphs in Fig. 3 show results of a comprehensive numerical search for maximum power using (4) by varying frequency, load resistance and K^2, while $Q = 400$ was kept constant. As a result maximum power, optimal load resistance and peak power frequencies as functions of K^2Q were found and plotted together with the analytic expressions for comparison and validation.

1) Peak Power Frequency: Fig. 3(a) shows the exact numerically found peak power frequency f_{peak}, the exact analytic expression for the branching point frequency f_{bp} (15), the approximate expression for the low-coupled range frequency

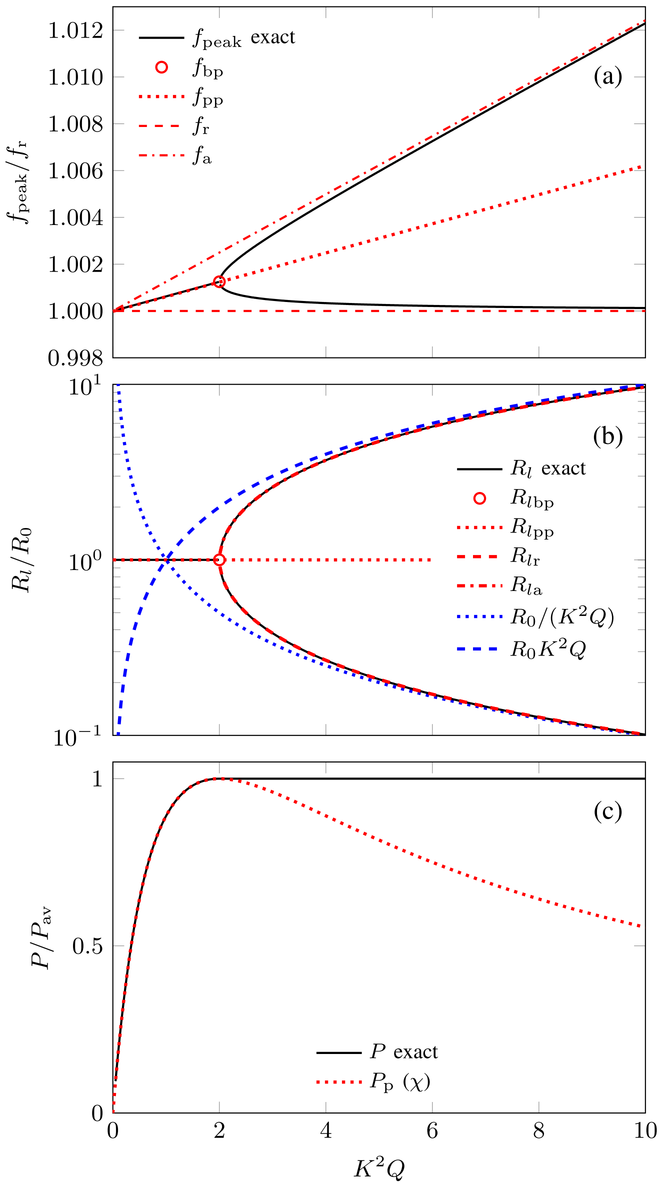

Fig. 3. Analysis of the exact and approximate analytic expressions in comparison with the exact results evaluated numerically from the power expression in (4). (a) Analysis of the peak power frequency. (b) Analysis of the optimal load values with maximum power transfer. (c) Analysis of the output power for the exact solution and the approximated solutions. $Q = 400$ is used for the evaluation.

f_{pp} (18) and the resonant (f_{r}) and anti-resonant frequencies (f_{a}). The plotted frequencies are all normalised to f_{r}. As predicted from the peak phase analysis in Fig. 2 there exist only a single optimal operating frequency in the low-coupled range $K^2Q < 2$. The analytic approximation in (18) for the peak power frequency in the low-coupled range f_{pp} shows fine agreement with the numerical analysis (f_{peak}), and f_{pp} is as predicted located midway between the resonant and anti-resonant frequency. The low-coupled approximation f_{pp} naturally only predicts the correct peak power frequency until the branching point $K^2Q = 2 + 1/Q$, where the peak power frequency f_{bp} is given by the exact expression in (15). For $K^2Q > 2$ the peak power frequency divides into two branches, one that approaches f_{r} and one that approaches f_{a} for increasing values of K^2Q. Fig. 3(a) clearly shows that an error is induced if approximating the peak power frequency of the two branches f_{pr} (resonant branch) and f_{pa} (anti-resonant branch) to be equal to f_{r} and f_{a} respectively. The error is however in most cases insignificant especially for high coupling, and for $K^2Q = 7$ which is approximately the coupling efficiency for the harvester presented in this work, the approximation error is hence less than 0.02%.

2) Optimal Load: Fig. 3(b) shows the exact optimal load R_l found from the numerical analysis of power expression (4) together with the analytic expressions for optimal loads for the branching point $R_{l\mathrm{bp}}$ (16), the low-coupled range $R_{l\mathrm{pp}}$ and the high-coupled range with $R_{l\mathrm{r}}$ near f_{r} and $R_{l\mathrm{a}}$ near f_{a}, where both load values are obtained from (20). The plotted optimal load values are all normalised to the impedance magnitude of the piezoelectric capacitor $R_0 = 1/(\omega_0 C)$. In the low-coupled range $K^2Q < 2$ with a single optimal load at the peak phase operating frequency f_{pp}, good agreement is observed between the exact numerical solution R_l and the analytic approximations for both $R_{l\mathrm{pp}}$ and the branching point optimal load $R_{l\mathrm{bp}}$ in (16). Similar as for the frequency analysis in Fig. 3(a), the optimal load divides into two branches for $K^2Q > 2$. The excellent agreement between the exact numerical solution R_l and the exact analytic values for $R_{l\mathrm{r}}$ and $R_{l\mathrm{a}}$ visibly validates the expression for $R_{l\mathrm{opt}}$ in (20).

While $R_{l\mathrm{opt}}$ is exact in the full high-coupled range, the expression in (20) can for simplicity be reduced to $R_{l\mathrm{r}} \simeq R_0/(K^2Q)$ and $R_{l\mathrm{a}} \simeq R_0K^2Q$ for sufficient high values of K^2Q. The reduced expressions are also plotted in Fig. 3(b) and shows that adequate precision is obtained for $K^2Q > 5$.

3) Output Power: The exact numerical solution to the output power of the harvester in (4) is seen in Fig. 3(c) where also the low-coupled approximation P_{p} in (19) is plotted. Whereas P_{p} shows excellent agreement with the exact solution in the low-coupled range, it naturally fails in its peak output power predictions for $K^2Q > 2$. With the power normalised to P_{av}, the exact solution in Fig. 3(c) illustrates that while increasing power can be extracted with increased coupling efficiency until $K^2Q = 2$, no additional power can be gained for stronger coupled systems. High coupled systems can, however, still be of interest since the high coupling reduces the optimal load value in the resonant branch. This may be preferable for design of the electrical system used in connection with the harvester.

From Fig. 3(c) it is clear that while the focus often is aimed towards optimising the parameters of the piezoelectric material, the important parameters concerning power are those included in P_{av} as long as $K^2Q > 2$. From (17) it thus directly follows that higher output power is achieved by increased mass and quality factor [24]. Under the assumption of constant acceleration, the output power is naturally increased for decreasing frequency but the resonant frequency is from an application point of view usually fixed by the targeted vibration source.

III. Fabrication

The fabrication of the unimorph energy harvesters is sketched in Fig. 4 and consists of a process with three conventional masking steps and one screen printing step.

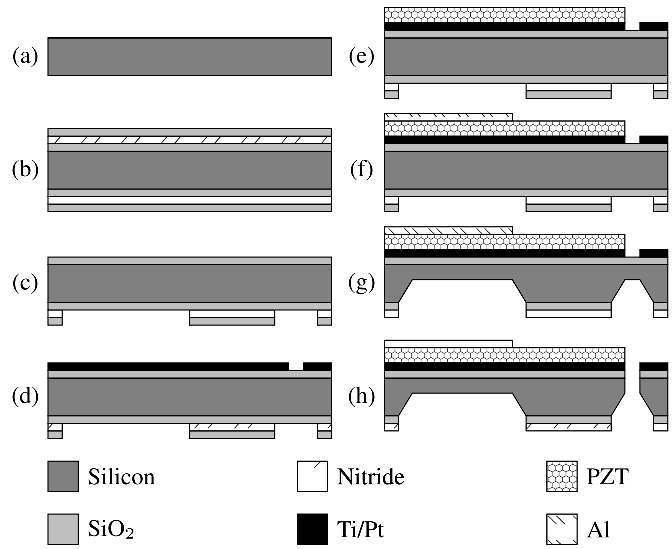

Fig. 4. Cross-sectional view of the fabrication process. (a) Double side polished 500 μm thick four inch diameter (001) silicon wafer. (b) 1 μm silicon dioxide, 170 nm stoichiometric silicon nitride and 300 nm LPCVD TEOS based silicon dioxide. (c) KOH mask windows defined by UV lithography and etching in bHF and hot phosphoric acid. (d) 50/500 nm Ti/Pt bottom electrode by e-beam evaporation, patterned by UV lithography and heated H_2O:HCl:HNO_3. (e) Screen printing of PZT thick film. (f) 600 nm Al top electrode by e-beam evaporation using a shadow mask. (g) Cavity etching in KOH with a mechanical front side protection. (h) Cantilever release in RIE.

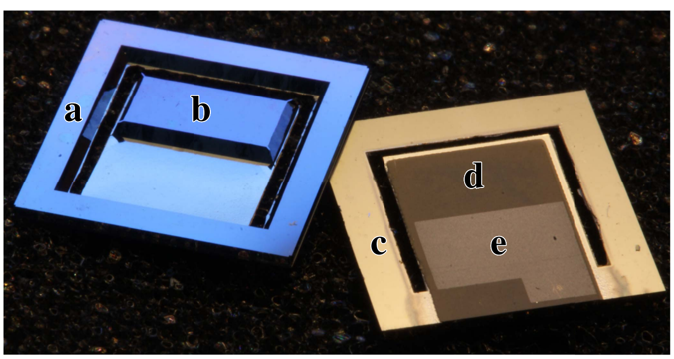

Fig. 5. Photograph showing front and back side of the fabricated energy harvester. (a) frame, (b) proof mass, (c) bottom electrode, (d) screen printed PZT thick film and (e) top electrode.

The starting point is a double side polished 500 µm thick four inch diameter (001) silicon wafer, Fig. 4(a). A 1 μm silicon dioxide (SiO_2) is grown in a wet thermal oxidation followed by low-pressure chemical vapor deposition (LPCVD) of 170 nm stoichiometric silicon nitride and a LPCVD of 300 nm SiO_2 based on tetraethyl orthosilicate (TEOS), Fig. 4(b). Mask windows for KOH etching on the backside are defined with UV lithography, while SiO_2 and silicon nitride are etched in buffered hydrofluoric acid (bHF) and 180 °C phosphoric acid (H_3PO_4), respectively, Fig. 4(c). A bottom electrode consisting of a 50 nm titanium adhesion layer and a 500 nm platinum layer, also serving as a diffusion barrier [25], is deposited using e-beam evaporation. The bottom electrode is patterned using UV lithography followed by a wet etch in 85 °C hot nitric-hydrochloric acid, H_2O:HCl:HNO_3 (8:7:1), Fig. 4(d). On top of the bottom electrode a 25 µm InSensor® TF2100 PZT thick film is deposited using screen printing, Fig. 4(e). Before the sintering process, the PZT thick film is high pressure treated to reduce the porosity [26]. As top electrode, a 600 nm aluminium layer is deposited using e-beam evaporation through a shadow mask, Fig. 4(f). The frontside of the wafer is protected using a mechanical holder while the SiO_2 is removed in bHF and the cavities are etched in 86 °C 28 wt% KOH, Fig. 4(g). The PZT structures are covered with photo-resist and the cantilevers are released by a SiO_2 etch in bHF followed by a reactive ion etch (RIE) of the silicon, Fig. 4(h). The wafers are diced and the PZT thick film of each device is polarised individually by applying an electric field between the top and bottom electrodes.

A photograph of two fabricated energy harvesters is shown in Fig. 5. The cantilever has integrated proof mass and anchoring and is enclosed by a silicon frame for stability and handling. The dimensions of the harvester are listed in Table I.

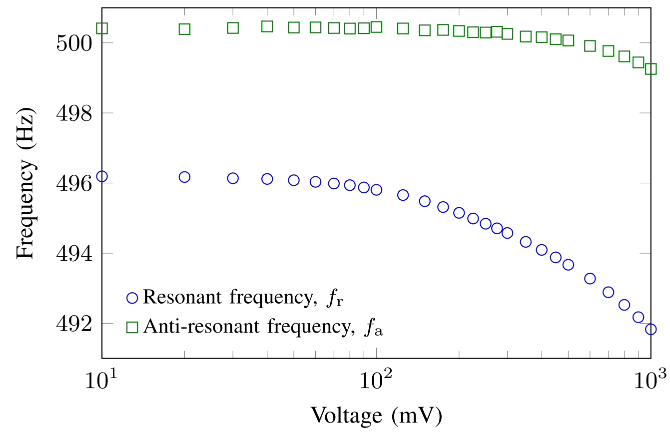

Fig. 6. Resonant and anti-resonant frequency as a function of measurement voltage amplitude. Theory only captures the linear regime with no mechanical softening effect.

TABLE I
DIMENSIONS OF THE FABRICATED VIBRATION ENERGY HARVESTER

Frame dimensions	10 mm × 10 mm
Medial dimension	< 1 mm
Cantilever width	6 mm
Cantilever length	3.25 mm
Si cantilever thickness	35 µm
PZT thickness	25 µm
Proof mass length	3.25 mm
Proof mass	22.4 mg
Total mass	26.6 mg

IV. EXPERIMENTAL RESULTS AND DISCUSSION

The evaluation of the performance of the fabricated MEMS-based energy harvester, serves also to validate experimentally the simple lumped element model by applying the impedance (6), voltage (3) and available power (17) expressions to measurement data. The experimental results will thus be accompanied by a parameter identification illustrating that the full harvester behaviour can be described using the five parameters C, f_r, K, m_{eff} and Q. The system coupling coefficient K can be calculated from the resonant and anti-resonant frequencies

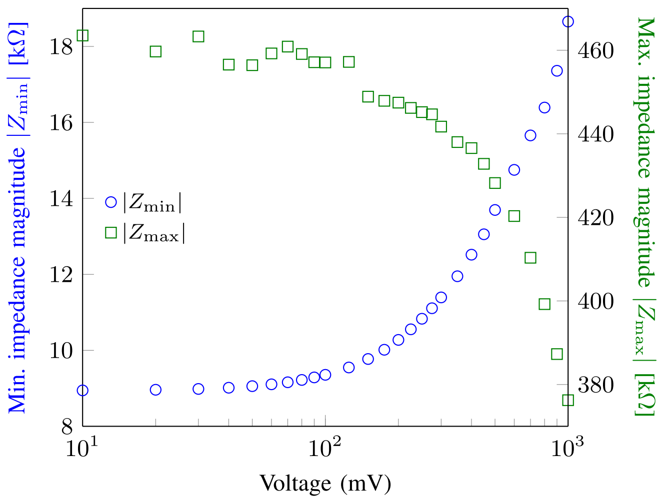

Fig. 7. Minimum and maximum impedance magnitudes as a function of measurement voltage amplitude. Increased minimum impedance magnitude indicates increased damping effects.

as

$$K^2 = \frac{f_a^2}{f_r^2} - 1 \tag{21}$$

and thus all five parameters can be derived experimentally using only electrical measurements.

The most common approach to determine the required parameters is using the direct piezoelectric effect and actuation from a shaker. The mechanical parameters f_r and Q can be determined by short circuiting the harvester while f_a is measured with the harvester in open circuit. C can be measured directly whereas m_{eff} either requires knowledge of the spring constant or it can be calculated or extracted by fitting the voltage expression (3) to the experimental data. Another and considerably faster approach is to measure the impedance magnitude and phase from which C, f_r, f_a and Q can be deducted in only one single swept frequency measurement.

A. Impedance Analysis

Using an Agilent 4294A Precision Impedance Analyzer the impedance of the harvester is measured by sweeping the frequency from low to high frequency using a sweep rate of $0.1\,\text{Hz}\,\text{s}^{-1}$. The SDOF model derived is only valid when the harvester is operated in the linear regime where neither spring hardening/softening or increased viscous damping occurs. Both non-linear phenomena are often seen in MEMS-based energy harvesters [27]–[29]. The non-linearity arises with increased deflection, and thus it also occurs for the high Q harvester presented in this work. Consequently it is required that the impedance measurements are carried out with an applied voltage that excites the harvester within its linear regime. Fig. 6 shows the resonant frequency and anti-resonant frequency, which are obtained from the minimum and maximum impedance magnitudes, respectively, as a function of applied voltage. The minimum and maximum impedance magnitudes are plotted in Fig. 7. The frequency plot in Fig. 6 clearly illustrates a significant softening effect where

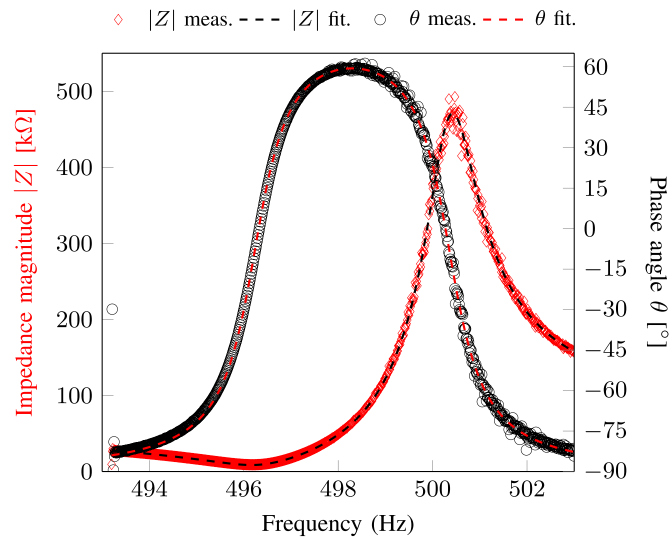

Fig. 8. Impedance and phase measured at an applied voltage of 10 mV. Circles represent the measurements while the solid line is the fitted impedance magnitude and phase from (6) with parameters listed in Table II.

TABLE II
EXTRACTED PARAMETERS FROM THE IMPEDANCE MAGNITUDE AND PHASE FIT IN FIG. 8

Capacitance, C	5.01 nF
Resonant frequency, f_r	496.24 Hz
Anti-resonant frequency, f_a	500.35 Hz
Quality factor, Q	441
$K = \sqrt{f_a^2/f_r^2 - 1}$	0.129
K^2Q	7.34

both f_r and f_a are decreasing for increasing applied voltage. The softening effect is more pronounced for f_r which is expected from the expression for the anti-resonant frequency $f_a = f_r\sqrt{1+K^2}$ and the definition of K in (8). As the softening effect decreases the spring constant, the system coupling coefficient K increases and accordingly compensates for the softening effect which is a mechanical phenomenon. While the frequency analysis extracted from the impedance measurements mainly provides information concerning the softening effect, the magnitude of the impedance contains direct information concerning the viscous damping. At the resonant frequency the mechanical impedance Z_m in the impedance expression (6) reduces to the viscous damping term. The significant increase in minimum impedance magnitude in Fig. 7 thus illustrates that the viscous damping must increase considerably resulting in a decrease in quality factor. The impedance measurement shown in Fig. 8 is hence performed with an applied voltage of 10 mV to minimise any non-linear effects. The expression for impedance in (6) is fitted to the measured data using a non-linear fitting routine with the resulting parameters listed in Table II. As evident from Fig. 8 the lumped parameter SDOF based model allows for accurate representation of the impedance, and if the harvester operates in the linear regime, four out of five parameters needed to describe the harvester performance can be extracted using this straightforward measurement.

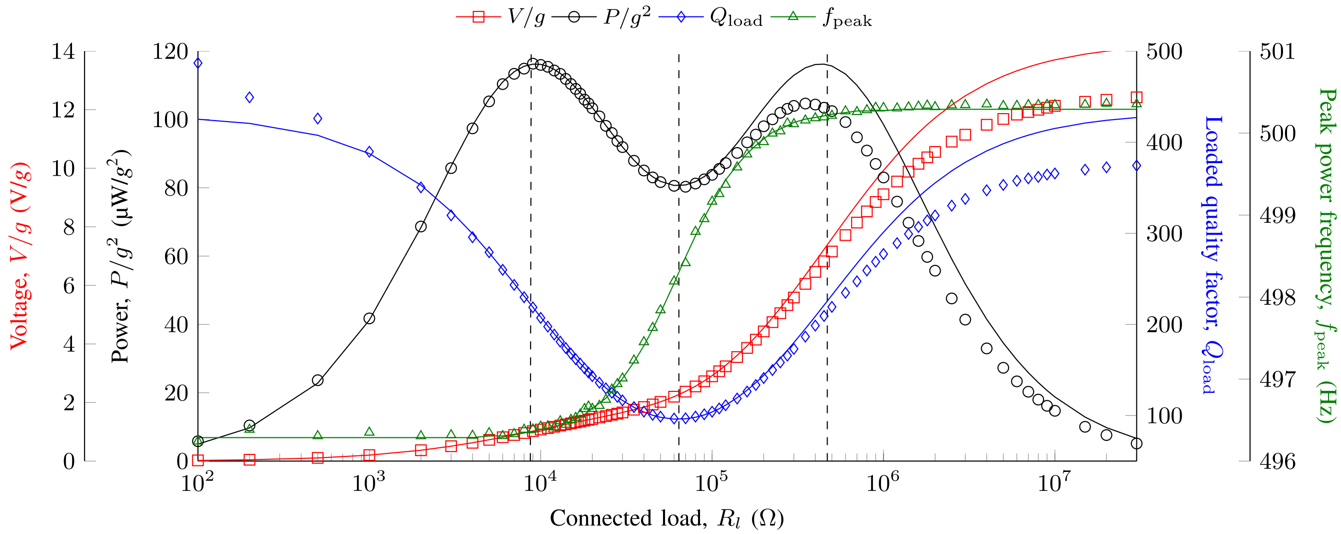

Fig. 9. Voltage, calculated power, loaded quality factor and peak power frequency as function of connected load resistance. Circles represent measurements while solid lines correspond to the derived SDOF lumped element model evaluated using the parameters listed in Table II under “Voltage fit”. The three vertical dashed lines indicate the load values of the two operating points of interest ($R_{l\mathrm{r}} = 8.7$ kΩ, $R_{l\mathrm{a}} = 470$ kΩ) and $R_0 = 64$ kΩ that corresponds to the local minimum between the two maxima. The measurements were performed at 10 mg RMS acceleration.

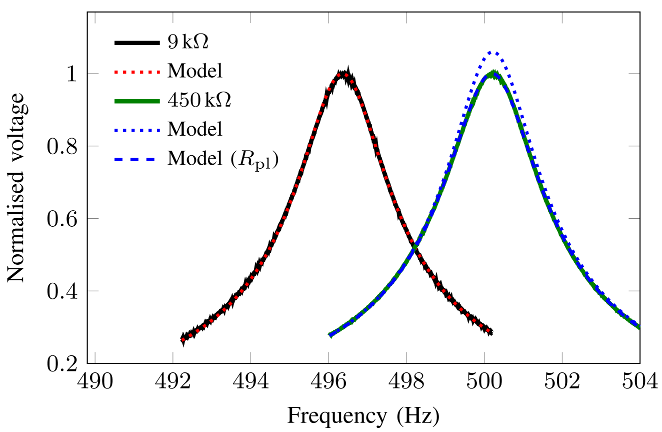

Fig. 10. Voltage responses for two different load values around $R_{l\mathrm{r}} = 9$ kΩ and $R_{l\mathrm{a}} = 450$ kΩ as a function of frequency. Voltage expression (3) fitted to 9 kΩ data results in the parameters listed in Table III. The model is evaluated at 450 kΩ with and without a parallel resistance accounting for leakage current. Measurements were performed at 10 mg RMS acceleration.

With Q and K^2 determined from the impedance measurements, the figure of merit K^2Q can be calculated to 7.34 and we are thus in the high-coupled regime with positive phase as seen in Fig. 8. Using the impedance magnitude of the capacitor $R_0 = 1/\omega_0 C = 64\,\mathrm{k\Omega}$ the two optimal load values with equal maximum power can be predicted to be $R_{l\mathrm{r}} = R_0/(K^2Q) = 8.7\,\mathrm{k\Omega}$ for the lower branch (f_r) and $R_{l\mathrm{a}} = R_0K^2Q = 470\,\mathrm{k\Omega}$ for the higher branch (f_a), see Fig. 3(b).

B. Optimal Load

To experimentally validate the existence of the two operating points with equal maximum power, the output power was measured for a range of loads. The harvester was actuated by a TV 51110 shaker system driven by a sinusoidal signal from an Agilent 33521A Function Generator. The acceleration was measured using a B&K Piezoelectric Accelerometer 8305 in connection with a B&K Type 2692-A-0I2 Charge Conditioner. The harvester was connected to a 1040 resistance box from Time Electronics and the generated voltage measured using a NI USB-6210 DAQ. The deflection of the cantilever was measured using an optoNCDT 2300 laser displacement sensor from Micro-Epsilon. The measurements were carried out at an RMS acceleration of 10 mg to minimise non-linear effects. The frequency was scanned from low to high frequency in a continuous sweep with a rate of $0.1\,\mathrm{Hz\,s^{-1}}$ and the frequency response was extracted from a synchronisation signal from the function generator. The peak voltage and peak deflection was obtained together with corresponding peak power frequency f_{peak} and the power was calculated as $P = V_{\mathrm{RMS}}^2/R_l$. The loaded quality factor was calculated from the power frequency spectrum as $Q_{\mathrm{load}} = f_{\mathrm{peak}}/f_{\mathrm{BW}}$ with f_{BW} being the full width at half maximum bandwidth. The results are seen in Fig. 9 where the voltage and power are normalised to input acceleration in gravitational unit $g = 9.82\,\mathrm{m^2\,s^{-1}}$ to first and second power, respectively.

TABLE III

PARAMETERS FROM THE IMPEDANCE MAGNITUDE AND PHASE FIT IN TABLE 2 TOGETHER WITH THE EXTRACTED PARAMETERS FROM THE VOLTAGE FIT IN FIG. 10

	Impedance fit	Voltage fit
Capacitance, C	5.01 nF	5.01 nF
Resonant frequency, f_r	496.24 Hz	496.28 Hz
Anti-resonant frequency, f_a	500.35 Hz	500.30 Hz
Quality factor, Q	441	430
$K = \sqrt{f_\mathrm{a}^2/f_\mathrm{r}^2 - 1}$	0.129	0.127
K^2Q	7.34	6.99
m_{eff}	-	$1.31 \times m_{\mathrm{total}}$
R_{pl}	-	3.7 MΩ

Except for Q_{load}, good agreement is observed between measurements and theory in the low range of load values. The discrepancy in Q_{load} at low load is mainly due to decreasing voltage signal to noise ratio. Whereas the measured output power follows the model predictions at the low optimal load

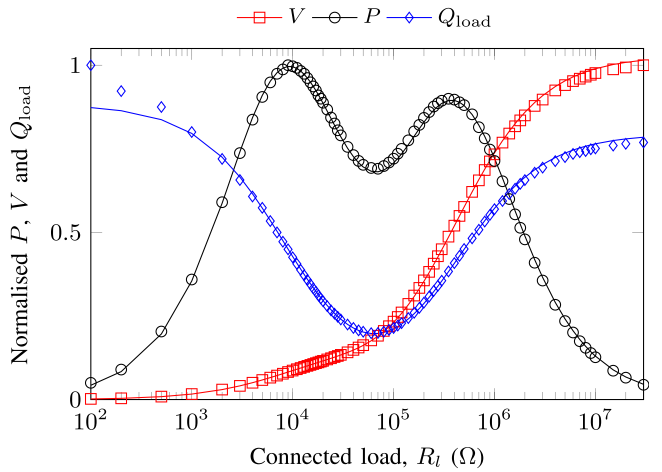

Fig. 11. Peak normalised voltage, power and loaded quality factor as function of connected load. The evaluated model represented by the solid lines is in comparison with Fig. 9 enhanced to include a parallel parasitic resistance of 3.7 MΩ to account for leakage current.

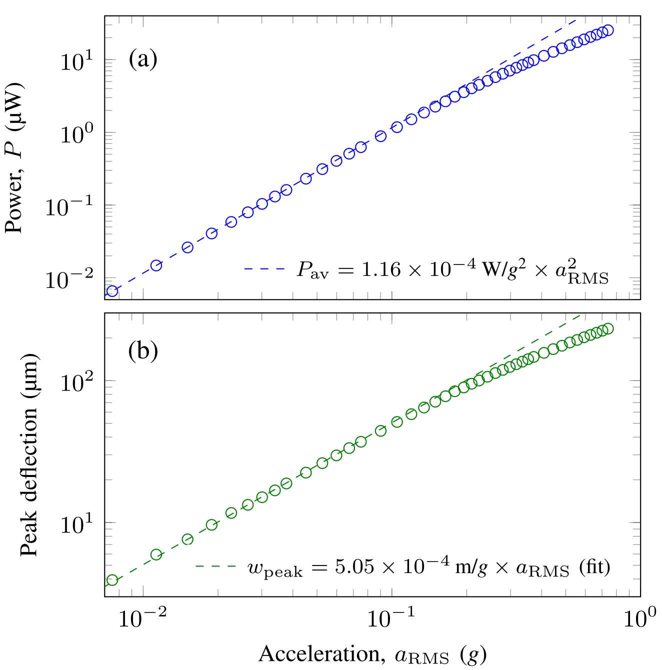

Fig. 12. Output power and peak deflection as function of input RMS acceleration measured in fractions of gravitational unit $g = 9.82\ \mathrm{m^2s^{-1}}$. A load resistance of 9 kΩ is used. (a) Dashed line indicates the analytical predicted power $P_{\rm av}$. (b) Dashed line represents a linear fit of the measured deflections up to 0.1 g.

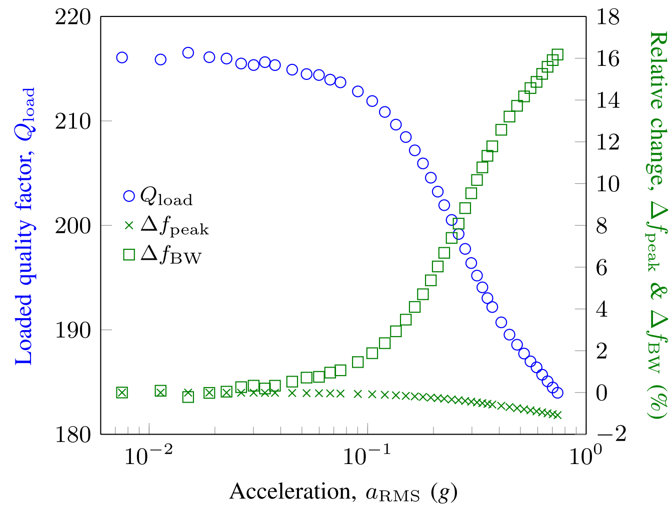

Fig. 13. Loaded quality factor and relative change of peak frequency and frequency response bandwidth as function of input acceleration. A load resistance of 9 kΩ is used.

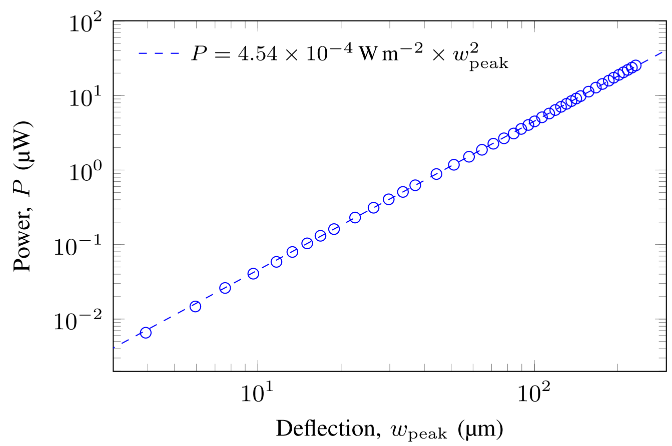

Fig. 14. Output power as function of the recorded peak deflection in Fig. 12. With the linear tendency it can be concluded that the non-linearities observed in Fig. 12(a) are due to mechanical and not electrical effects. Dashed line represents a second order fit with corresponding listed coefficient.

value R_{lr} and also exhibits a local minimum at R_0, a clear discrepancy is observed for both power, voltage and loaded quality factor for increasing load values. The measured voltage becomes increasingly lower than expected at higher load values and consequently the measured power is less than predicted. The loaded quality factor at short and open circuit is expected to correspond to the mechanical quality factor which is approximately equal at short and open circuit due to a relative frequency difference of only $\approx 1\%$. $Q_{\rm load}$ at high load is however around 10% lower than expected, indicating a damping contribution at open circuit not accounted for in the model. The evaluation of the model is based on the equivalent circuit diagram in Fig. 1 and it is hence assumed that the piezoelectric layer contributes to the electrical circuit only with a capacitor. This assumption is not perfect, since the piezoelectric layer is not a valid dielectric and a certain leakage current is expected to pass the layer.

C. Leakage Current

The parameters used in the model evaluation in Fig. 9 are listed in Table III in the *Voltage fit* column. While the capacitance for the voltage fit is obtained from the impedance fit parameters listed in Table II, the values for $f_{\rm r}$, $f_{\rm a}$ and Q are changed slightly due to differences in non-linear effects and measurement uncertainties between the impedance analyser and shaker measurements. From the voltage fit the effective mass can be estimated as $1.31 \times m_{\rm total}$ where $m_{\rm total} = 26.6\,\mathrm{mg}$ is the total mass of the cantilever and proof mass.

As seen in Fig. 10, the model and measurements show excellent agreement for the voltage frequency response at

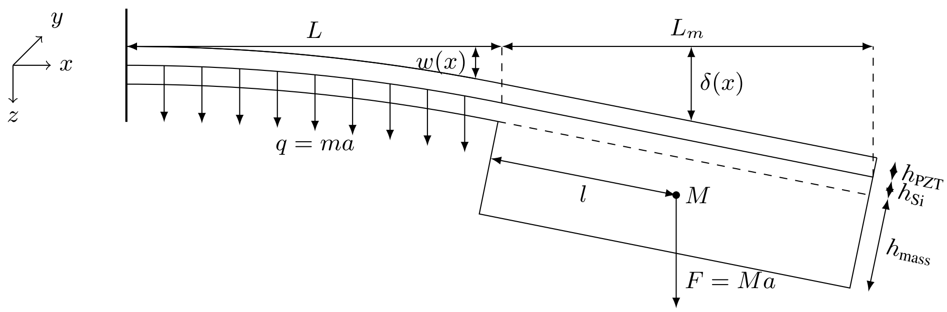

Fig. 15. Schematic cross-section of the unimorph vibration energy harvester. The thin part of the cantilever with length L consist of a silicon support layer of thickness h_{Si} and a PZT layer of thickness h_{PZT}. The thin part of the cantilever continues into the integrated proof mass with length L_m where the thickness of the proof mass h_{mass} is equal to the silicon wafer thickness minus h_{Si}. The force on the proof mass F is assumed to act on the proof mass midpoint $l = L_m/2$, which also is assumed to be the SDOF system centre of mass.

the $9\,\mathrm{k\Omega}$ low load resistance value, whereas at the $450\,\mathrm{k\Omega}$ high load resistance measurement the voltage is lower than predicted. By including in the model a parasitic resistor, R_{pl} in parallel with the piezoelectric capacitor C, the leakage current in the piezoelectric layer can be accounted for. By fitting the R_{pl} model to the $450\,\mathrm{k\Omega}$ data with all other parameters constant, a parasitic resistance of $R_{\mathrm{pl}} = 3.7\,\mathrm{M\Omega}$ is extracted. The effective resistance connected to the harvester then becomes $401\,\mathrm{k\Omega}$ instead of $450\,\mathrm{k\Omega}$ and agreement is observed between measured voltage response and model.

Using the modified model with the parallel parasitic resistance of $3.7\,\mathrm{M\Omega}$ in the full range of loads in Fig. 9 the modified optimal load characteristic in Fig. 11 is obtained. Agreement is now observed between the model and measured values of voltage, power and loaded quality factor in the full range of connected loads.

D. Power Performance

As observed in the impedance measurements in Figs. 6 and 7 the harvester performance is affected by non-linear effects at increased excitation. These non-linear effects will also occur when examining the power performance for increasing levels of input acceleration. Since the leakage current in the piezoelectric layer causes a loss in power dissipation in the external connected load at the high load optimum, the focus is towards the performance at the low load optimum. Fig. 12(a) shows the frequency tracked peak output power in a $9\,\mathrm{k\Omega}$ load as function of input RMS acceleration. Since $K^2Q \simeq 7$ the output power equals the available power (17) and by using the values for m_{eff}, Q and f_{r} from the voltage fit in Table III, the output power can be calculated to $P = P_{\mathrm{av}} = 1.16 \times 10^{-4}\mathrm{W}/g^2 \times a_{\mathrm{RMS}}^2$.

As evident from Fig. 12(a) the measured power is in accordance with predictions until around $0.1\,g$ where the power becomes less than predicted. A similar tendency is observed for the recorded peak deflection in Fig. 12(b) and thus indicates that, despite the optimal load value for $R_{l\mathrm{r}}$ increases for higher excitation according to Fig. 7, the loss in power is mainly due to decreased deflection.

This conclusion is substantiated by examining the loaded quality factor as function of input acceleration in Fig. 13. It must be stressed that strictly speaking the concept of quality factor applies only for linear resonators with symmetric frequency response functions, hence the values for low and high accelerations are not directly comparable. Fig. 13 therefore also holds the relative change of the peak power frequency and bandwidth. The peak power frequency decreases by around 1% over the acceleration range and shows the softening effects also observed in the impedance analysis in Fig. 6. In the same acceleration range the bandwidth increases by 16% indicating a significant increase in damping factor, and with the loaded quality factor depending linearly on both peak frequency and bandwidth, the reason for the decreasing Q_{load} is mainly the increased damping in the system.

The loss of proportionality between power and acceleration squared in Fig. 12(a) can potentially also arise partly from non-linear effects in the electrical properties of the harvester. This is examined in Fig. 14 where the power is plotted as function of peak deflection. The power is observed to increase in agreement with the deflection squared, and thus is can be concluded that the non-linearity observed in power performance at higher acceleration originates solely from mechanical effects. Secondly, while the load ideally should be adjusted at increasing accelerations, the effect is small compared to the reduced deflection due to increased mechanical damping.

V. Conclusion

With focus on the piezoelectric device impedance we have revisited the standard SDOF mass-spring-damper based electromechanical model of a piezoelectric vibration energy harvester. Instead of the conventional mathematical derivative approach the piezoelectric impedance was used in the theoretical analysis of peak power frequency, optimal load and output power.

By dividing the theoretical analysis into three cases: the low-coupled case ($K^2Q < 2$), the branching point case ($K^2Q = 2 + 1/Q$), and the high-coupled case ($K^2Q > 2$), closed form expressions were presented for the full range of K^2Q values. A closed form approximate power expression was elaborated for the low-coupled case and excellent agreement was observed in comparison with the exact numerical solution. In the low-coupled regime with a single optimal operating frequency and load value, the output power increases with increasing K^2Q until the branching point where the output power of the harvester becomes equal to the available power of the resonator. At the branching point the harvester moves from a single optimal operating point to two optimal operating points with equal output power but with two different load resistances and peak power frequencies. With the output power being equal to the available power no additional power can be extracted from the resonator for stronger coupled systems ($K^2Q > 2$). Stronger coupled systems can only benefit from relatively lower optimal load values.

From characterisation of a high-coupled unimorph MEMS-based PZT thick film harvester it was validated that the impedance and voltage expressions of SDOF model accurately represents the harvester performance. Using the indirect piezoelectric effect it was shown how four of five lumped parameters in the SDOF model can be determined experimentally from a single impedance measurement scan. The remaining parameter, the effective mass, must be determined using a shaker measurement and the direct piezoelectric effect. With focus on the piezoelectric impedance it is thus possible to accurately determine all five lumped parameters using solely electrical probing, and with only two measurement sweeps required the characterisation effort is considerably reduced.

While the simple model accurately represents the voltage and power at the low optimal load resistance, disagreement was observed for the high optimal load resistance. It was found necessary to implement a parasitic resistance of 3.7 MΩ in parallel with the piezoelectric capacitance to account for leakage current. The power performance of the harvester was measured to 11.7 nW at 10mg with a load of 9 kΩ at 496.3 Hz corresponding to 117μW/g^2.

With $K^2Q \simeq 7$ for the fabricated harvester, the output power can only be increased by increasing the available power of the resonator. The resonant frequency for vibration harvesters are usually determined by the vibration source while the quality factor is a trade-off between high peak power and narrow bandwidth. The mass is thus the main parameter of interest for optimisation of high-coupled harvesters.

APPENDIX A

A. Coupling Coefficient Γ

The coupling coefficient Γ relating current with deflection slope rate and induced moment with voltage is found from the piezoelectric constitutive equations [30], [31] and Euler-Bernoulli beam theory. The cantilever comprising the unimorph vibration energy harvester is sketched in Fig. 15. With the cantilever length and width being considerable larger than the thickness, plane stress is assumed. Accordingly, the normal and shear stresses are neglectable while only the strain S_1 is non-zero [32]. Likewise only the electric field normal to the electrodes ($E_z = E_3$) is considered with the electric displacement being divergence free ($\nabla \cdot \mathbf{D} = 0$). By using the following effective material parameters for compliance s^E, piezoelectric constant d and permittivity ε^T

$$s^E = s_{11}^E - s_{11}^E \nu^2 \tag{22a}$$

$$d = d_{31} + d_{31}\nu \tag{22b}$$

$$\varepsilon^T = \varepsilon_{33}^T - \frac{d_{31}^2}{s_{11}^E}\nu \tag{22c}$$

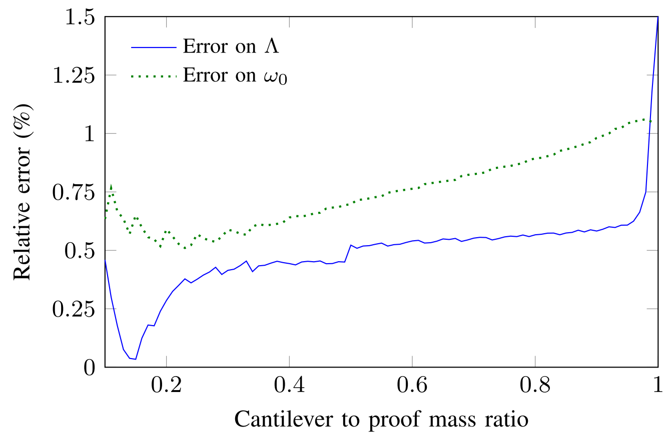

Fig. 16. Error in analytically predicted geometric length factor Γ and resonant frequency ω_0 relative to finite element modelling. The error is plotted as function of cantilever to proof mass ratio, with a value of 1 equalling a cantilever without proof mass.

where s_{ij}^E is the elastic compliance at constant or zero electric field, d_{31} the piezoelectric constant, ε_{33}^T the z-component of the dielectric permittivity at constant or zero stress and $\nu = s_{12}^E/s_{11}^E$ the Poisson's ratio, the constitutive equations can be expressed as $S_1 = dE_3 + s^E T_1$ and $D_3 = \varepsilon^T E_3 + dT_1$ with S_i and T_i being the components of the strain and stress vectors and D_3 the z-component of the electric displacement.

It is assumed that the thin part of the cantilever undergoes pure bending, hence the geometrical strain can be expressed as $S_1 = -zw''_{xx}$ where w is the deflection and z the position relative to the neutral axis of the beam. The generated charge Q on the electrodes of the piezoelectric layer can be determined by integrating the displacement field D_3 over the active volume of the piezoelectric layer divided by the layer thickness. The current I can followingly be expressed as $I = \dot{Q} = \Gamma \dot{w}'_x(L) + C\dot{V}$ with $\dot{X}$ being shorthand for $\partial X/\partial t$, C the total capacitance including additional parasitic capacitances, V the voltage, $w'_x(L)$ the deflection slope at L and Γ the coupling coefficient

$$\Gamma = \left(d/s_{\mathrm{PZT}}^E\right)(h_{\mathrm{PZT}} - 2h_0)\,W/2, \tag{23}$$

where W is the width of the cantilever, s_{PZT}^E the effective compliance for the PZT material and h_0 is the material interface position relative to neutral axis (25).

B. Characteristic Length Factor Λ

The characteristic length factor $\Lambda = w_c/w'_x(L)$ describes the relation between vertical centre of mass displacement of the SDOF system and deflection slope at distance L. The Λ factor is derived from Euler-Bernoulli beam equation using the boundary conditions $w(0) = 0$, $w'_x(0) = 0$ and that the proof mass acts as a bending moment of Fl at the proof mass joint of distance L. The asymmetry of the proof mass relative to the neutral axis is neglected, as are any rotational effects of the proof mass. The proof mass is assumed completely rigid hence the deflection slope of the proof mass follows

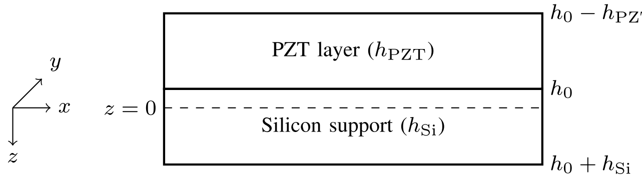

Fig. 17. Sketch of the neutral plane position in a unimorph cantilever consisting of a joined silicon support and a PZT layer with equal thickness. The distance from neutral axis at $z = 0$ where no strain is present to the material interface is denoted h_0, from which correct integration limits can be defined.

the deflection slope at the proof mass joint $w_x'(L)$. The centre of mass for the SDOF system is approximated to be at the proof mass midpoint l and thus the centre of mass deflection becomes $w_c = w(L) + l w_x'(L)$. It then follows that

$$\Lambda = \frac{L^2(4l + 3L)m + 8\left(3l^2 + 3lL + L^2\right)M}{4\left(L^2 m + 6lM + 3LM\right)} \tag{24}$$

where $M = WL_m((h_{\mathrm{Si}} + h_{\mathrm{mass}})\rho_{\mathrm{Si}} + h_{\mathrm{PZT}}\rho_{\mathrm{PZT}})$ is the proof mass and $m = W(h_{\mathrm{Si}}\rho_{\mathrm{Si}} + h_{\mathrm{PZT}}\rho_{\mathrm{PZT}})$ is the mass per unit length of the thin part of the cantilever with ρ_{Si} and ρ_{PZT} being the respective material densities for silicon and PZT. The analytically predicted Λ factor in (24) is verified in Fig. 16 as the error relative to a finite element model (FEM).

The FEM simulation is performed in Comsol® with the silicon support being modelled as an anisotropic material. The error is plotted as function of cantilever to proof mass ratio for a constant total cantilever length. A ratio of 1 hence means a harvester with no proof mass and vice versa for a ratio approaching 0. For the cantilever to proof mass ratio of 0.5 for the harvester fabricated in this work, an error of 0.5% relative to FEM is obtained.

Fig. 16 also shows the error of the analytically predicted angular resonant frequency ω_0 relative to that calculated using FEM as function of cantilever to proof mass ratio. The angular resonant frequency is derived from the Rayleigh-Ritz maximum energy method [33]. The error is seen to be less than 1% in most of the cantilever to proof mass interval illustrated in Fig. 16.

C. Neutral Axis h_0

The material interface h_0 (see sketched unimorph cantilever in Fig. 17) is found by analysing the longitudinal forces. Since pure bending is assumed, the sum of all normal forces in x-direction on the cantilever cross section is zero when subjecting the cantilever to an external bending moment ($\sum F_{x,\perp} = 0$).

Integrating over the stresses in each of the materials using the limits from Fig. 17 and ignoring the electric field in the PZT layer due to a short-circuit condition, the following expression for h_0 is deduced

$$h_0 = \frac{-h_{\mathrm{Si}}^2 s_{\mathrm{PZT}}^E + h_{\mathrm{PZT}}^2 s_{\mathrm{Si}}}{2\left(h_{\mathrm{Si}} s_{\mathrm{PZT}}^E + h_{\mathrm{PZT}} s_{\mathrm{Si}}\right)}. \tag{25}$$

References

[1] N. S. Hudak and G. G. Amatucci, "Small-scale energy harvesting through thermoelectric, vibration, and radiofrequency power conversion," *J. Appl. Phys.*, vol. 103, no. 10, pp. 101301-1–101301-24, May 2008.

[2] R. Vullers, R. van Schaijk, I. Doms, C. Van Hoof, and R. Mertens, "Micropower energy harvesting," *Solid-State Electron.*, vol. 53, no. 7, pp. 684–693, Jul. 2009.

[3] A. Harb, "Energy harvesting: State-of-the-art," *Renew. Energy*, vol. 36, no. 10, pp. 2641–2654, Oct. 2011.

[4] S. P. Beeby, M. J. Tudor, and N. M. White, "Energy harvesting vibration sources for microsystems applications," *Meas. Sci. Technol.*, vol. 17, no. 12, pp. R175–R195, Dec. 2006.

[5] A. Erturk and D. J. Inman, "A distributed parameter electromechanical model for cantilevered piezoelectric energy harvesters," *J. Vibrat. Acoust.*, vol. 130, no. 4, pp. 041002-1–041002-15, 2008.

[6] N. G. Elvin and A. A. Elvin, "A general equivalent circuit model for piezoelectric generators," *J. Intell. Mater. Syst. Struct.*, vol. 20, no. 1, pp. 3–9, Jan. 2009.

[7] A. Erturk and D. J. Inman, "An experimentally validated bimorph cantilever model for piezoelectric energy harvesting from base excitations," *Smart Mater. Struct.*, vol. 18, no. 2, p. 025009, Feb. 2009.

[8] P. Bonello and S. Rafique, "Modeling and analysis of piezoelectric energy harvesting beams using the dynamic stiffness and analytical modal analysis methods," *J. Vibrat. Acoust.*, vol. 133, no. 1, pp. 011009-1–011009-11, Feb. 2011.

[9] F. Goldschmidtboeing, M. Wischke, C. Eichhorn, and P. Woias, "Parameter identification for resonant piezoelectric energy harvesters in the low- and high-coupling regimes," *J. Micromech. Microeng.*, vol. 21, no. 4, pp. 045006–045016, Apr. 2011.

[10] R. Elfrink, M. Renaud, T. M. Kamel, C. de Nooijer, M. Jambunathan, M. Goedbloed, *et al.*, "Vacuum-packaged piezoelectric vibration energy harvesters: Damping contributions and autonomy for a wireless sensor system," *J. Micromech. Microeng.*, vol. 20, no. 10, pp. 104001-1–104001-7, Oct. 2010.

[11] E. Aktakka, R. Peterson, and K. Najafi, "Thinned-PZT on SOI process and design optimization for piezoelectric inertial energy harvesting," in *Proc. 16th Int. Solid-State Sens., Actuators Microsyst. Conf.*, Bejing, China, Jun. 2011, pp. 1649–1652.

[12] D. Shen, J.-H. Park, J. H. Noh, S.-Y. Choe, S.-H. Kim, H. C. Wikle, *et al.*, "Micromachined PZT cantilever based on SOI structure for low frequency vibration energy harvesting," *Sens. Actuators A, Phys.*, vol. 154, no. 1, pp. 103–108, Aug. 2009.

[13] A. Lei, R. Xu, A. Thyssen, A. Stoot, T. Christiansen, K. Hansen, *et al.*, "MEMS-based thick film PZT vibrational energy harvester," in *Proc. IEEE 24th Int. Conf. MEMS*, Cancún, Quintana Roo, Mexico, Jan. 2011, pp. 125–128.

[14] S. Roundy, P. K. Wright, and J. Rabaey, "A study of low level vibrations as a power source for wireless sensor nodes," *Comput. Commun.*, vol. 26, no. 11, pp. 1131–1144, Jul. 2003.

[15] R. Lou-Moeller, C. C. Hindrichsen, L. H. Thamdrup, T. Bove, E. Ringgaard, A. F. Pedersen, *et al.* "Screen-printed piezoceramic thick films for miniaturised devices," *J. Electroceram.*, vol. 19, no. 4, pp. 333–338, Mar. 2007.

[16] J. M. Renno, M. F. Daqaq, and D. J. Inman, "On the optimal energy harvesting from a vibration source," *J. Sound Vibrat.*, vol. 320, nos. 1–2, pp. 386–405, Feb. 2009.

[17] M. Renaud, R. Elfrink, M. Jambunathan, C. de Nooijer, Z. Wang, M. Rovers, *et al.*, "Optimum power and efficiency of piezoelectric vibration energy harvesters with sinusoidal and random vibrations," *J. Micromech. Microeng.*, vol. 22, no. 10, pp. 105030–105042, Oct. 2012.

[18] T. M. Kamel, R. Elfrink, M. Renaud, D. Hohlfeld, M. Goedbloed, C. de Nooijer, *et al.*, "Modeling and characterization of MEMS-based piezoelectric harvesting devices," *J. Micromech. Microeng.*, vol. 20, no. 10, p. 105023, Oct. 2010.

[19] N. Kong, D. S. Ha, A. Erturk, and D. J. Inman, "Resistive impedance matching circuit for piezoelectric energy harvesting," *J. Intell. Mater. Syst. Struct.*, vol. 21, no. 13, pp. 1293–1302, 2010.

[20] A. Dompierre, S. Vengallatore, and L. G. Frechette, "Theoretical and practical limits of power density for piezoelectric vibration energy harvesters," in *Proc. Power MEMS*, Seoul, Republic of Korea, 2011, pp. 249–252.

[21] C. Williams and R. Yates, "Analysis of a micro-electric generator for microsystems," *Sens. Actuators A, Phys.*, vol. 52, nos. 1–3, pp. 8–11, Mar. 1996.

[22] P. Mitcheson, T. Green, E. Yeatman, and A. Holmes, "Architectures for vibration-driven micropower generators," *J. Microelectromech. Syst.*, vol. 13, no. 3, pp. 429–440, Jun. 2004.

[23] D. Guyomar, A. Badel, E. Lefeuvre, and C. Richard, "Toward energy harvesting using active materials and conversion improvement by non-linear processing," *IEEE Trans. Ultrason., Ferroelectr. Freq. Control*, vol. 52, no. 4, pp. 584–595, Apr. 2005.

[24] N. E. Dutoit, B. L. Wardle, and S.-G. Kim, "Design considerations for MEMS-scale piezoelectric mechanical vibration energy harvesters," *Integr. Ferroelectr.*, vol. 71, no. 1, pp. 121–160, Jul. 2005.

[25] C. C. Hindrichsen, T. Pedersen, E. V. Thomsen, K. Hansen, and R. Lou-Moeller, "Investigation of top/bottom electrode and diffusion barrier layer for PZT thick film MEMS sensors," *Ferroelectr.*, vol. 367, no. 1, pp. 201–213, 2008.

[26] C. G. Hindrichsen, R. Lou-Moeller, K. Hansen, and E. V. Thomsen, "Advantages of PZT thick film for MEMS sensors," *Sens. Actuators A, Phys.*, vol. 163, no. 1, pp. 9–14, 2010.

[27] R. Elfrink, T. M. Kamel, M. Goedbloed, S. Matova, D. Hohlfeld, Y. van Andel, *et al.*, "Vibration energy harvesting with aluminum nitride-based piezoelectric devices," *J. Micromech. Microeng.*, vol. 19, no. 9, p. 094005, Sep. 2009.

[28] R. Xu, A. Lei, C. Dahl-Petersen, K. Hansen, M. Guizzetti, K. Birkelund, *et al.*, "Fabrication and characterization of MEMS-based PZT/PZT bimorph thick film vibration energy harvesters," *J. Micromech. Microeng.*, vol. 22, no. 9, p. 094007, Sep. 2012.

[29] R. Xu, A. Lei, C. Dahl-Petersen, K. Hansen, M. Guizzetti, K. Birkelund, *et al.*, "Screen printed PZT/PZT thick film bimorph MEMS cantilever device for vibration energy harvesting," *Sens. Actuators A, Phys.*, vol. 188, pp. 383–388, Dec. 2012.

[30] *IEEE Standard on Piezoelectricity*, ANSI/IEEE Standard 176-1987, 1988.

[31] J. Smits and W.-S. Choi, "The constituent equations of piezoelectric heterogeneous bimorphs," *IEEE Trans. Ultrason., Ferroelectr. Freq. Control*, vol. 38, no. 3, pp. 256–270, May 1991.

[32] E. Tadmor and G. Kosa, "Electromechanical coupling correction for piezoelectric layered beams," *J. Microelectromech. Syst.*, vol. 12, no. 6, pp. 899–906, 2003.

[33] S. D. Senturia, *Microsystem Design*. Boston, MA, USA: Kluwer, 2001.

Anders Lei received the B.Sc.(E) and M.Sc.(E) degrees in physics and nanotechnology, and the Ph.D. degree in microelectromechanical systems from the Technical University of Denmark (DTU), Lyngby, Denmark, in 2007, 2009, and 2013, respectively.

In 2013 he joined the MEMS-AppliedSensors group at DTU Nanotech as Postdoc, working with fabrication of ultrasound transducers using both piezoelectric thick films and silicon micromachining.

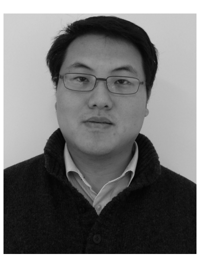

Ruichao Xu received his B.Sc. degree and M.Sc. degree in applied physics from the Technical University of Denmark (DTU), Lyngby, Denmark, in 2007 and 2009, respectively. He received his Ph.D. degree in the field of MEMS at the Department of Micro- and Nanotechnology (DTU Nanotech) in 2012.

He has worked on various projects during his study ranging from sunsensors on CubeSats to the development and fabrication of microreactors for catalysis. In 2012 he joined the R&D department at Meggitt A/S in Kvistgaard, Denmark, and worked on several projects, including energy harvesting.

He has been on the management board of the Electrical Engineering Society of Denmark (E-gruppen) since 2007, most recently as vice chairman.

Louise M. Borregaard received the M.Sc. degree in physics and nanotechnology from the Technical University of Denmark (DTU), Lyngby, Denmark, in 2011.

At DTU she was involved in several MEMS projects including energy harvesting and the fabrication of micro direct methanol fuel cells. In 2011 Louise joined Meggitt A/S, Denmark, working as a Research Engineer on projects involving energy harvesting and ultrasonic devices. Her research interests include processing of PZT thick films and development of piezoelectric materials and devices.

Michele Guizzetti was born in Italy, in 1981. He received the degree in electronics engineering and the Ph.D. degree in electronic instrumentation from the University of Brescia, Brescia, Italy, in 2006 and 2011, respectively.

Until August 2010, he collaborated with the Department of Information Engineering of the University of Brescia on research activities dealing with power harvesting and autonomous systems. In particular he was involved with piezoelectric and thermoelectric energy conversion. Now he is employed as Senior Research Engineer at Meggitt A/S, Denmark, working on projects regarding power harvesting.

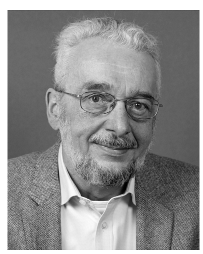

Ole Hansen received the M.Sc. degree in microtechnology from the Technical University of Denmark (DTU), Lyngby, Denmark, in 1977.

Since 1977 he has worked with micro and nanotechnology and applications of the technology within electronics, metrology, sensing, catalysis and energy harvesting. He is Professor at DTU Nanotech, the Technical University of Denmark, where he is heading the Silicon Microtechnology group, with activities within lithography based micro- and nanotechnology. Current research interests include photocatalysis and tools for characterizing catalytic processes. Since 2005 he has been part of the Danish National Research Foundation Center, Center for Individual Nanoparticle Functionality, Technical University of Denmark.

Erik V. Thomsen was born in Aarhus, Denmark, in 1964. He received the M.Sc. degree in physics from Odense University, Odense, Denmark, and the Ph.D. degree in electrical engineering from the Technical University of Denmark (DTU), Lyngby, in 1998.

He has been affiliated with the Department for Micro and Nanotechnology, DTU, since 1992. In 2008, he became a Professor. Since 2003, he has been group leader for the MEMS Applied Sensors Group. His current research and teaching interests include MEMS multisensors; bio-medical devices; small scale energy systems, such as miniature fuel cells and energy harvesting devices; capacitive micromachined ultrasonic transducers; and piezoelectric MEMS. He teaches classes in solid-state electronics, microtechnology, and nano- and microfabrication.

Dr. Thomsen received the AEG Electron Prize in 1995 and has also received several teaching awards at DTU.